

Higher Chest X-ray Resolution Improves Classification Performance

Alessandro Wollek^a, Sardi Hyska^b, Bastian Sabel^b, Michael Ingrischi^b,
Tobias Lasser^a

^a*Munich Institute of Biomedical Engineering, and School of Computation, Information,
and Technology, Technical University of Munich, Boltzmannstr.*

11, Garching, 85748, Bavaria, Germany

^b*Department of Radiology, University Hospital*

Ludwig-Maximilians-University, Marchioninistr. 15, Munich, 81337, Bavaria, Germany

Abstract

Deep learning models for image classification are often trained at a resolution of 224×224 pixels for historical and efficiency reasons. However, chest X-rays are acquired at a much higher resolution to display subtle pathologies. This study investigates the effect of training resolution on chest X-ray classification performance, using the chest X-ray 14 dataset. The results show that training with a higher image resolution, specifically 1024×1024 pixels, results in the best overall classification performance with a mean AUC of 84.2 % compared to 82.7 % when trained with 256×256 pixel images. Additionally, comparison of bounding boxes and GradCAM saliency maps suggest that low resolutions, such as 256×256 pixels, are insufficient for identifying small pathologies and force the model to use spurious discriminating features. Our code is publicly available at <https://gitlab.lrz.de/IP/cxr-resolution>.

Keywords: image resolution, chest X-ray, chest radiograph, object detection, classification, saliency map

1. Introduction

Since AlexNet, images processed by deep learning models are often resized to 224×224 pixels during training mostly for computational reasons (Krizhevsky et al., 2012; He et al., 2016; Huang et al., 2017; Tan and Le, 2020; Wollek et al., 2023). Training at a lower resolution requires less memory and consequently models train faster. However, lowering the resolution

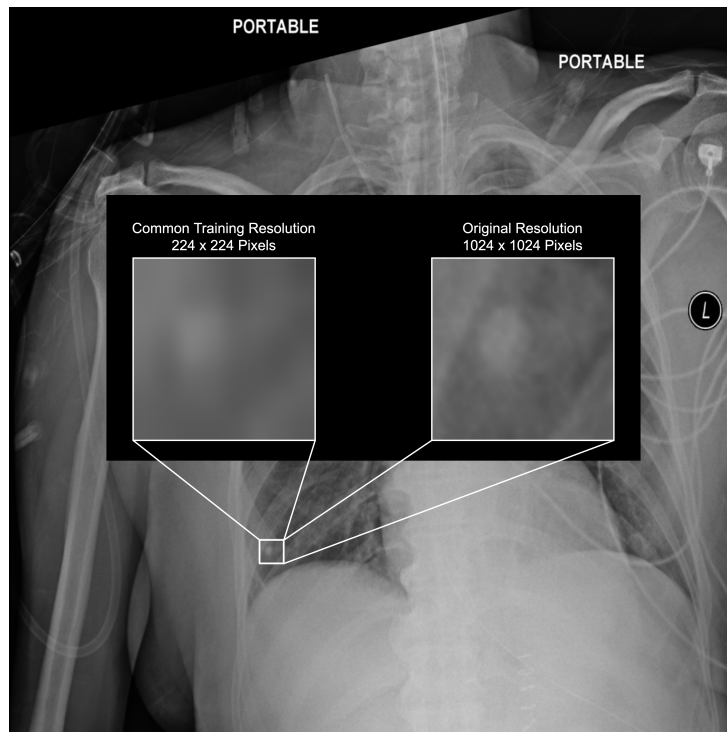


Figure 1: Chest X-ray classification models are commonly trained at a 224×224 pixel resolution for historical and efficiency reasons. Chest X-rays, on the other hand, are acquired with a high resolution to display subtle features. As a consequence, at a lower resolution, a small nodule (highlighted in the white bounding box) becomes blurred and almost invisible.

can also blur or occlude important regions of an image, as shown in Figure 1.

Tan and Le (2020) studied the importance of image resolution on image classification accuracy using the ImageNet data set (Deng et al., 2009). They concluded that image resolution is a hyper-parameter similar to network depth or width. For chest radiographs, Sabottke and Spieler (2020a) tested different image resolutions (32×32 up to 600×600 pixels) on the task of chest X-ray classification. In their experiments, maximum classification AUCs were obtained between 256×256 and 448×448 pixel resolution. While their results suggest that a 448×448 pixel resolution is sufficient, chest radiographs have a much higher resolution. For example, the images in the MIMIC data set have an average resolution of 2500×3500 pixels (Johnson et al., 2019). To close this research gap, we investigate the effect of image resolution on chest X-ray classification performance. Our contributions are:

- We systematically analyze the effect of image resolution on chest X-ray classification performance from 64×64 up to 1024×1024 pixels, the highest resolution available.
- We show that training with the highest available resolution, 1024×1024 pixels, achieves the highest classification performance on average and for most classes (11/14).
- By analyzing saliency map-extracted bounding boxes, we provide evidence that training at a lower resolution encourages the network to learn spurious discriminating features, potentially eroding trust into the (correct) prediction.

2. Materials and Methods

2.1. Data Set

For our experiments we chose the publicly available chest X-ray 14 data set containing 112,120 frontal view chest radiographs from 32,717 patients (Wang et al., 2017). The chest radiographs were annotated according to the 14 labels atelectasis, cardiomegaly, consolidation, edema, effusion, emphysema, fibrosis, hernia, infiltration, mass, nodule, pleural thickening, pneumonia, and pneumothorax. We selected this data set specifically as the authors provide a small test sub set (983 images) with bounding box annotations for eight of the 14 classes (atelectasis, cardiomegaly, effusion, infiltration, mass, nodule,

Class	Training	Validation	Test
Atelectasis	7996	1119	2420
Cardiomegaly	1950	240	582
Consolidation	3263	447	957
Edema	1690	200	413
Effusion	9261	1292	2754
Emphysema	1799	208	509
Fibrosis	1158	166	362
Hernia	144	41	42
Infiltration	13914	2018	3938
Mass	3988	625	1133
Nodule	4375	613	1335
Pleural Thickening	2279	372	734
Pneumonia	978	133	242
Pneumothorax	3705	504	1089

Table 1: Class distributions of the data set used in this study.

Finding	Bounding Box Area (px^2)	#Samples
Nodule	5,527	18
Atelectasis	33,753	43
Mass	50,083	20
Pneumothorax	55,208	18
Effusion	61,901	30
Infiltration	119,563	25
Pneumonia	159,466	22
Cardiomegaly	184,134	28

Table 2: Mean bounding box area per class in squared pixels. Annotated samples stem from the provided test split.

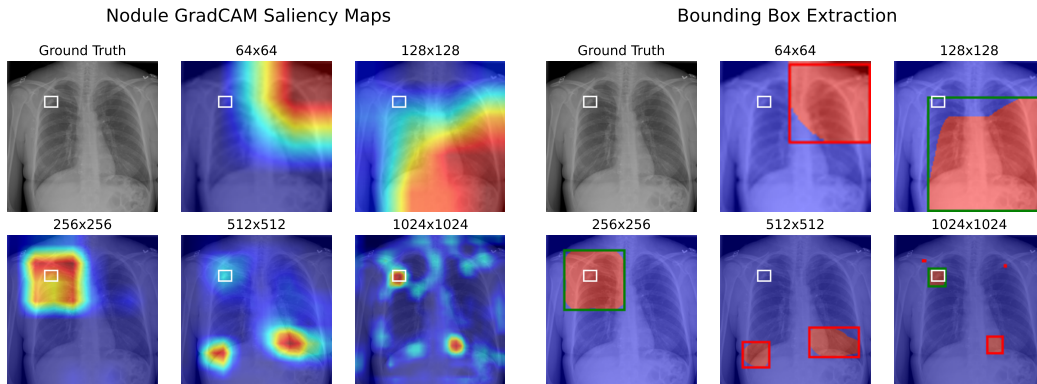
pneumonia, and pneumothorax). For training, we used the data split provided by the authors. The class distributions are reported in Table 1. While the images of the chest X-ray 14 data set were down-scaled to 1024×1024 pixels before their release (Wang et al., 2017), it is the only large, publicly available data set that also contains bounding boxes (see Table 2).

2.2. Chest X-ray Classification

For classification, we used the current state-of-the-art for chest X-ray classification (Xiao et al., 2023), a DenseNet-121 (Huang et al., 2017) pre-trained on the ImageNet data set. To predict the 14 classes, we replaced the last layer with a 14-dimensional fully-connected layer. Before model training, images were resized if necessary. For our experiments, we investigated the resolutions 64×64 , 128×128 , 256×256 , 512×512 , and the highest available resolution, 1024×1024 pixels. We trained every model with binary cross entropy loss, AdamW (Loshchilov and Hutter, 2018) optimization with default parameters, a learning rate of 0.0003, and a weight decay of 0.0001. We divided the learning rate by a factor of ten if the validation loss did not improve after two epochs and stopped the training if the validation loss did not improve after ten epochs. At a resolution of 64×64 pixels we used a batch size of 64, for 1024×1024 pixels of 12, and otherwise of 16. For each model we selected the best checkpoint based on the validation area under the receiver operating curve (AUC). We measured the effect of image resolution on chest X-ray classification using the AUC.

2.3. Object Detection

Given the bounding box annotations for eight of the 14 classes, we investigated the effect of image resolution on predicted bounding boxes by comparing extracted saliency maps to the bounding box annotations. We created segmentations from GradCAM (Selvaraju et al., 2017) saliency maps (see Figure 2a). Saliency maps were extracted from the penultimate layer, normalized, and converted to a binary representation by applying a threshold of 0.5. For bounding box creation, we extracted the connected components and calculated the surrounding bounding boxes, as shown in Figure 2b. For each class we measured the mean precision and accuracy. The precision is defined as the number of true positives divided by the number of detections (Padilla et al., 2020). Since the chest X-ray 14 data set contains only one bounding box per sample, the precision is either 0 or 1 over the number of



(a) GradCAM saliency maps for nodule classification (white bounding box) trained with different training resolutions.

(b) Saliency map-generated bounding boxes for nodule classification. Ground truth-overlapping detections surrounded in green, otherwise in red.

Figure 2: Saliency map-extracted bounding boxes for measuring the effect of image resolution on the model’s basis of decision making.

detections. A detection was considered positive if the intersection over union (IoU) was at least 0.1. The IoU is defined as

$$\text{IoU}(A, B) = \frac{A \cap B}{A \cup B},$$

where A and B are two bounding boxes. Out of multiple sufficiently overlapping detections only one was considered as a true positive.

3. Results

3.1. Chest X-ray Classification

Per-class chest X-ray classification AUC scores are provided in Table 3. Unsurprisingly, the model trained on only 64×64 pixel images scored the lowest, with a mean AUC of 77.5 %. The highest resolution, 1024×1024 pixels, performed best with a mean AUC of 84.2 %, followed by 256×256 pixels with a mean AUC of 82.7 %.

3.2. Object Detection

Examples of the effect of image resolution on generated saliency maps are provided in Figure 3. When increasing the image resolution, the generated GradCAM saliency maps become more granular due to the larger activation size.

Finding	Resolution				
	64×64	128×128	256×256	512×512	1024×1024
Atelectasis	0.760	0.800	0.810	0.807	0.821
Cardiomegaly	0.858	0.900	0.906	0.909	0.908
Consolidation	0.752	0.787	0.797	0.794	0.797
Edema	0.866	0.869	0.885	0.878	0.891
Effusion	0.845	0.873	0.877	0.874	0.879
Emphysema	0.824	0.884	0.900	0.913	0.937
Fibrosis	0.748	0.803	0.816	0.821	0.850
Hernia	0.865	0.926	0.903	0.895	0.916
Infiltration	0.678	0.707	0.714	0.699	0.714
Mass	0.765	0.827	0.830	0.813	0.829
Nodule	0.669	0.719	0.761	0.780	0.803
Pleural Thickening	0.730	0.751	0.757	0.763	0.796
Pneumonia	0.688	0.743	0.760	0.760	0.769
Pneumothorax	0.799	0.839	0.858	0.859	0.877
Mean	0.775	0.816	0.827	0.826	0.842

Table 3: Chest X-ray classification AUCs for different image resolutions. Highest values are highlighted in bold.

Finding	64×64	128×128	256×256	512×512	1024×1024
Nodule	0.000	0.000	0.000	0.150	0.326
Atelectasis	0.001	0.117	0.120	0.361	0.395
Mass	0.004	0.003	0.330	0.417	0.508
Pneumothorax	0.003	0.061	0.391	0.180	0.198
Effusion	0.004	0.036	0.310	0.353	0.356
Infiltration	0.008	0.283	0.084	0.201	0.200
Pneumonia	0.095	0.370	0.189	0.394	0.402
Cardiomegaly	0.114	0.804	0.946	0.792	0.242
Mean	0.029	0.209	0.296	0.356	0.328

Table 4: Mean precision at intersection over union $\geq 10\%$ of chest pathology detections. Findings ordered by average ground truth bounding box size.

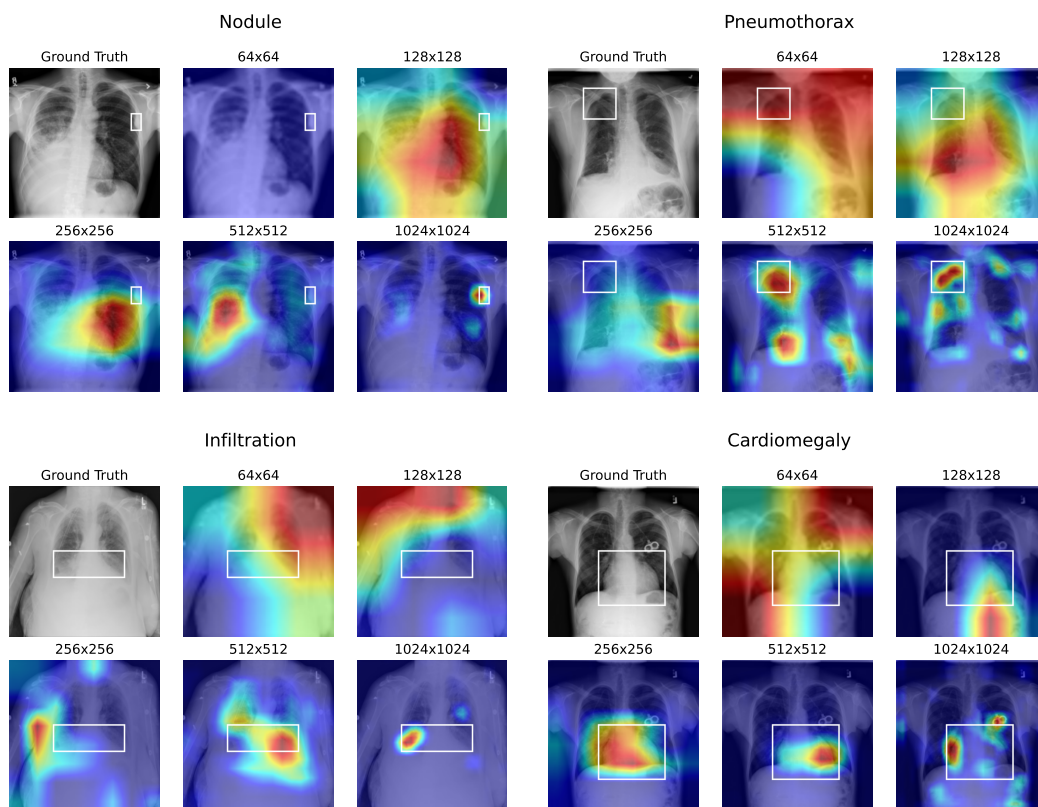


Figure 3: Generated saliency maps when trained with different resolutions for nodule (a), pneumothorax (b), infiltration (c), and cardiomegaly (d) classification (ground truth marked in the white bounding box).

Finding	64x64	128x128	256x256	512x512	1024x1024
Nodule	0.000	0.000	0.000	0.278	0.611
Atelectasis	0.070	0.140	0.256	0.605	0.488
Mass	0.100	0.150	0.500	0.550	0.600
Pneumothorax	0.167	0.222	0.500	0.389	0.556
Effusion	0.233	0.200	0.600	0.833	0.567
Infiltration	0.440	0.520	0.360	0.440	0.200
Pneumonia	0.227	0.455	0.727	0.591	0.591
Cardiomegaly	0.643	0.857	0.964	0.964	0.536

Table 5: Bounding box detection accuracy at intersection over union greater or equal to 0.1. Rows ordered by average bounding box size.

Mean precision @ IoU ≥ 0.1 results for pathology detection are reported in Table 4, ordered by average ground truth bounding box size. For 5 of 8 classes the highest resolution, 1024×1024 pixels, scored the highest precision, except for cardiomegaly, infiltration, and pneumothorax, where 256×256 (cardiomegaly, pneumothorax) and 128×128 (infiltration) performed best. For the three smallest pathologies, nodule, atelectasis, and mass, the highest resolution strongly outperformed the others. Especially for the smallest pathology, nodule, the mean precision was non-zero only for the resolutions 512×512 and 1024×1024 pixels. Noticeably, the largest pathology, cardiomegaly, was best detected according to the saliency maps at a resolution of 256×256 and second to worst at 1024×1024 pixels. However, training 1024×1024 pixel resolutions achieved a classification AUC of 90.8 % compared to 90.6 % when training with 256×256 pixel images, see Table 3.

Mean detection accuracy results, ignoring multiple detections, are reported in Table 5. Similarly to the mean precision results, higher resolutions (512×512 , 1024×1024) achieved a higher accuracy for smaller bounding boxes, and lower resolutions (128×128 , 256×256) for larger bounding boxes. On average, the highest accuracy was measured when trained with 512×512 pixel images.

4. Discussion

We investigated the importance of chest X-ray resolution on classification performance motivated by small pathologies that become indistinguishable on low resolution images (see Figure 1).

The classification results show that overall a higher resolution improves image classification performance (see Table 3). On average, the highest available resolution, 1024×1024 , performed best with an AUC of 84.2% compared to a common resolution of 256×256 pixels with an AUC of 82.7 %. While Sabottke and Spieler (2020b) achieved maximum AUCs between 256×256 and 448×448 pixels resolution, they tested only up to 600×600 pixels. We also observed a slight decline in AUC from 256×256 to 512×512 pixel resolution for most (9/14) classes. These findings are in line with their conclusion that a resolution 600×600 was not optimal. However, our results show that an even higher image resolution, 1024×1024 pixels, improved chest X-ray classification performance. Similar results were obtained for image classification accuracy on ImageNet (Tan and Le, 2020).

Surprisingly, even a resolution as low as 64×64 pixels achieved an classification AUC of 77.5 %. While one could argue that this result suggests that training at a lower resolution is a sensible performance trade-off for faster training, inspecting the saliency maps draws a different picture. For example, the mean precision and accuracy detection results for the smallest pathology, nodule, surpass zero only at a resolution of 512×512 or higher (see Tables 4 and 5). On the one side, this is due to the intersection over union threshold that penalizes very large bounding boxes (see Figure 2b). On the other side, both quantitative results and visual inspection showed that the models attend to incorrect places for the prediction at a lower resolution (see examples in Figure 3). We interpret these results as that the model is forced to learn spurious distinctive features if the resolution is not sufficient. While the detection performance decreased for larger bounding boxes when trained at a higher resolution, these models (512×512 and 1024×1024) still achieved the highest classification AUCs. Inspecting the saliency maps revealed that, for example, for cardiomegaly, the models attended to the correct regions but focused only on fractions of the area surrounded by the ground truth bounding boxes. Considering both classification and detection results show that training at a higher resolution, for example 1024×1024 is preferable.

Our study has several limitations. First, we measured the importance of resolution on basis of decision making by comparing saliency maps to bounding boxes. Given more bounding box annotated data and encouraged by our results, a future study will investigate the effect of image resolution on detection performance. Second, our experimental setup tested only resolutions up to the highest available resolution of 1024×1024 pixels.

In conclusion, we investigated the effect of image resolution on chest X-

ray classification. We showed that training at a higher resolution than conventionally, 1024×1024 pixels, achieves a higher classification performance. Furthermore, our results suggest that training at a lower but common resolution of 256×256 pixels poses the risk of encouraging the model to base its prediction on spurious features.

5. Acknowledgments

This work was supported in part by the German federal ministry of health’s program for digital innovations for the improvement of patient-centered care in healthcare [grant agreement no. 2520DAT920].

References

- Deng, J., Dong, W., Socher, R., Li, L.J., Li, K., Fei-Fei, L., 2009. ImageNet: A large-scale hierarchical image database, in: 2009 IEEE Conference on Computer Vision and Pattern Recognition, pp. 248–255. doi:10.1109/CVPR.2009.5206848.
- He, K., Zhang, X., Ren, S., Sun, J., 2016. Deep residual learning for image recognition, in: Proceedings of the IEEE Conference on Computer Vision and Pattern Recognition, pp. 770–778.
- Huang, G., Liu, Z., Van Der Maaten, L., Weinberger, K.Q., 2017. Densely connected convolutional networks, in: Proceedings of the IEEE Conference on Computer Vision and Pattern Recognition, pp. 4700–4708. arXiv:1608.06993.
- Johnson, A.E., Pollard, T.J., Berkowitz, S.J., Greenbaum, N.R., Lungren, M.P., Deng, C.y., Mark, R.G., Horng, S., 2019. MIMIC-CXR, a de-identified publicly available database of chest radiographs with free-text reports. Scientific Data 6.
- Krizhevsky, A., Sutskever, I., Hinton, G.E., 2012. Imagenet classification with deep convolutional neural networks. Advances in neural information processing systems 25, 1097–1105.
- Loshchilov, I., Hutter, F., 2018. Decoupled Weight Decay Regularization, in: International Conference on Learning Representations.

- Padilla, R., Netto, S.L., da Silva, E.A., 2020. A survey on performance metrics for object-detection algorithms, in: 2020 International Conference on Systems, Signals and Image Processing (IWSSIP), IEEE. pp. 237–242.
- Sabottke, C.F., Spieler, B.M., 2020a. The Effect of Image Resolution on Deep Learning in Radiography. *Radiology: Artificial Intelligence* 2, e190015. doi:10.1148/ryai.2019190015.
- Sabottke, C.F., Spieler, B.M., 2020b. The Effect of Image Resolution on Deep Learning in Radiography. *Radiology: Artificial Intelligence* 2, e190015. doi:10.1148/ryai.2019190015.
- Selvaraju, R.R., Cogswell, M., Das, A., Vedantam, R., Parikh, D., Batra, D., 2017. Grad-CAM: Visual Explanations From Deep Networks via Gradient-Based Localization, in: Proceedings of the IEEE International Conference on Computer Vision, pp. 618–626.
- Tan, M., Le, Q.V., 2020. EfficientNet: Rethinking Model Scaling for Convolutional Neural Networks. arXiv:1905.11946 [cs, stat] arXiv:1905.11946.
- Wang, X., Peng, Y., Lu, L., Lu, Z., Bagheri, M., Summers, R.M., 2017. ChestX-ray8: Hospital-scale Chest X-ray Database and Benchmarks on Weakly-Supervised Classification and Localization of Common Thorax Diseases, in: 2017 IEEE Conference on Computer Vision and Pattern Recognition (CVPR), pp. 3462–3471. doi:10.1109/CVPR.2017.369, arXiv:1705.02315.
- Wollek, A., Graf, R., Čečátka, S., Fink, N., Willem, T., Sabel, B.O., Lasser, T., 2023. Attention-based Saliency Maps Improve Interpretability of Pneumothorax Classification. *Radiology: Artificial Intelligence* , e220187doi:10.1148/ryai.220187.
- Xiao, J., Bai, Y., Yuille, A., Zhou, Z., 2023. Delving into masked autoencoders for multi-label thorax disease classification, in: Proceedings of the IEEE/CVF Winter Conference on Applications of Computer Vision, pp. 3588–3600.